Effect of deposition pressure on the microstructure and electrochromic properties of electron-beam-evaporated nickel oxide films

Anoop Agrawal, Hamid R. Habibi*, Raj K. Agrawal*, John P. Cronin and Dale M. Roberts*

Donnelly Corporation, Advanced Technology Center, 4545 East Fort Lowell Road, Tucson, AZ 85712-1108 (USA)

R'Sue Caron-Popowich[†] and Carl M. Lampert

Energy and Environment Division, Lawrence Berkeley Laboratory, 1 Cyclotron Road (MS 62-203), Berkeley, CA 94720 (USA)

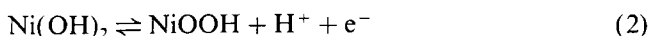(Received May 20, 1992; accepted July 14, 1992)

Abstract

Electron-beam-evaporated nickel oxide films were shown to have a microcrystalline cubic nickel oxide structure. The pressure in the chamber during the film deposition has a large effect on the crystal size and the stoichiometry of the films. The redox currents, the efficiency of these films to color, and their optical properties were influenced by the processing conditions employed and the resulting microstructure. A model is proposed based on the observed microstructure that explains the source of overstoichiometric oxygen and ion transport in these films.
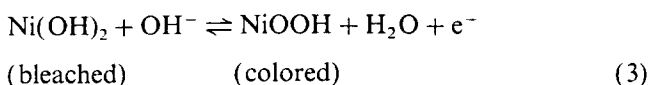
1. Introduction

Electrochromic devices for large-area displays, smart windows and automotive rearview mirrors are of considerable technological and commercial interest [1, 2]. Typically these devices are either multiple-layer stacks that are sequentially vacuum deposited or laminate constructions. Nickel oxide is used as one of the active electrochromic layers. It has been proposed that coloration occurs when the nickel oxide film is oxidized to nickel oxyhydroxide as shown below [3, 4]:

$$NiO + OH^- \rightleftharpoons NiOOH + e^- \qquad (1)$$

(bleached)   (colored)
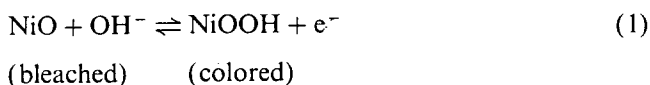
Alternatively, it has been suggested that the electrochromic properties arise owing to a small quantity of nickel hydroxide which may be present in the nickel oxide films. Proposed mechanisms for this reaction would be [5, 6]

$$Ni(OH)_2 \rightleftharpoons NiOOH + H^+ + e^- \qquad (2)$$

or

$$Ni(OH)_2 + OH^- \rightleftharpoons NiOOH + H_2O + e^- \qquad (3)$$

(bleached)   (colored)

To resolve which of these reactions takes place, it is important to understand the chemical composition of the films. This study was directed towards understanding the physical and chemical microstructure, electrochemical and electrochromic properties of electron-beam-deposited nickel oxide films as a function of deposition pressure.

2. Experimental details

The films were deposited from nickel oxide powder onto various substrates by electron beam evaporation at normal incidence. The total average pressure (mainly nitrogen) during the evaporation process in the chamber for the samples was as given in Table 1.

The film thickness measured by a step profilometer for the three samples was 50 nm, 49 nm and 42 nm respectively. The films were coated on pyrolytic carbon, on glass, on glass coated with indium tin oxide (ITO) and on transmission electron microscopy (TEM) copper grids required for the different experimental procedures described below.

2.1. X-ray photoelectron spectroscopy

The composition of the nickel oxide films was analyzed using a Perkin–Elmer PHI 5100 X-ray photoelectron spectroscopy (XPS) system using Mg Kα radiation. The pressure in the sample compartment during the measurement was 1.3×10^{-7} Pa. Measurements were carried out at take-off angles of 1.31 and

TABLE 1. Total average pressure during the evaporation process in the chamber for the samples

Sample	Pressure during deposition (Pa)
A	6.7×10^{-2}
B	1.3×10^{-2}
C	2.7×10^{-4}

0.35 rad in order to compare the chemical species present in the top few atomic layers with those in the bulk film. The results reported have been corrected for carbon at 285 eV and for satellites arising from the $K\alpha_2$ radiation.

2.2. Rutherford backscattering

Rutherford backscattering spectroscopy (RBS) was carried out on samples deposited on a smooth graphite substrate with a pyrolytic carbon coating obtained from Ultra Carbon Corporation in Bay City, MI. The RBS equipment consisted of a 5.5 MeV Van de Graaff generator with a 600 MeV AMU bending magnet. A quadrupole lens was used to focus the beam on the target. Backscattering was measured at 2.97 rad. The detector (Si–Li surface barrier) was located 0.15 m away from the target and extended a solid angle of 0.78 msterad. The pressure in the target chamber was maintained by dry nitrogen at 2.7×10^{-4} Pa. The incoming beam of ^{4}He had an energy of 1892 keV.

2.3. X-ray diffraction

X-ray diffraction was performed on single-layer nickel oxide films deposited on soda–lime glass using a Rigaku diffractometer. The angle between the incoming Cu Kα beam and the substrate was fixed at 0.026 rad.

2.4. Transmission electron microscopy

Nickel oxide was evaporated directly on carbon-coated copper TEM grids and on ITO-coated glass to observe the cross-section of these specimens. The samples for cross-section were prepared in the following way: nickel oxide samples coated on ITO glass were cut to 2 mm × 10 mm using a diamond saw. With coated sides facing each other, pairs of pieces were bonded together with epoxy, set in a metal clamp to ensure minimum epoxy bond line thickness and cured at 90 °C for 1 h. Discs 3 mm in diameter were cut from the bonded material, ground flat and polished on one side. The other side was dimpled and polished to perforation. Final thinning was done at liquid-nitrogen temperature by ion milling from both sides at an angle of 0.21 rad with 5 kV argon ions and a total beam current of 0.5 mA. Care was taken to minimize the heating of the material during specimen preparation, but it should be noted that, in addition to the epoxy curing step

described above, the material may have been exposed to excessive heat for periods during the ion-milling process. It was necessary to evaporate a layer of carbon onto the surface to prevent the charge build-up on the insulating glass surface. A third type of sample was prepared by scraping the coating deposited on an ITO-coated glass substrate and pressing the powder onto a carbon-coated TEM grid. All samples on copper grids were imaged on a JEOL 100 CX at 100 kV. Other samples were examined in a Philips 400 electron microscope operated at 100 kV.

2.5. Cyclic voltammetry and electrochromic measurements

Cyclic voltammetry was performed using a BAS CV-27 cyclic voltammeter. Films were cycled using a triangular waveform in 1 N KOH solution in a standard three-electrode configuration consisting of the sample as the working electrode, a conventional saturated calomel electrode (SCE) configuration immersed in saturated KCl solution as the reference electrode, and a high purity platinum mesh as the counterelectrode. Connection between the working and reference electrode compartments was made by a porous glass membrane and a Luggin capillary. Unless stated otherwise, potentials are quoted with respect to the SCE reference. All voltammograms were taken at room temperature in a quiescent solution. Optical measurements were performed on a Perkin–Elmer Lambda 7 spectrometer.

3. Results and discussion

3.1. Chemical identity

A typical multiplex (XPS) scan of a nickel oxide coating (sample B) is shown in Fig. 1. The surface primarily consists of nickel, oxygen and carbon.

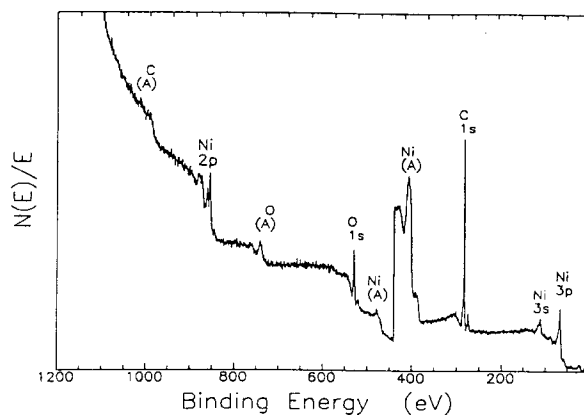As shown in Fig. 2(a), the binding energy of Ni 2p electrons in the metallic state is quite different from that
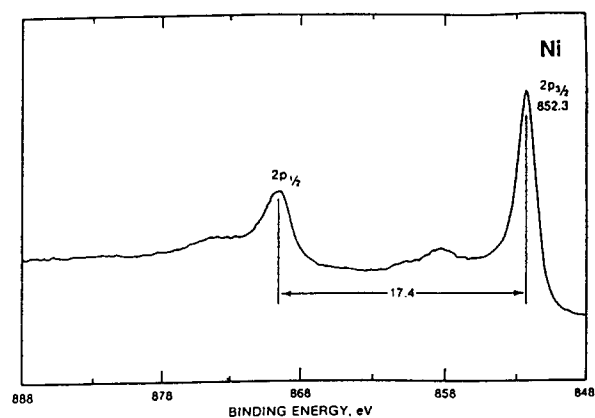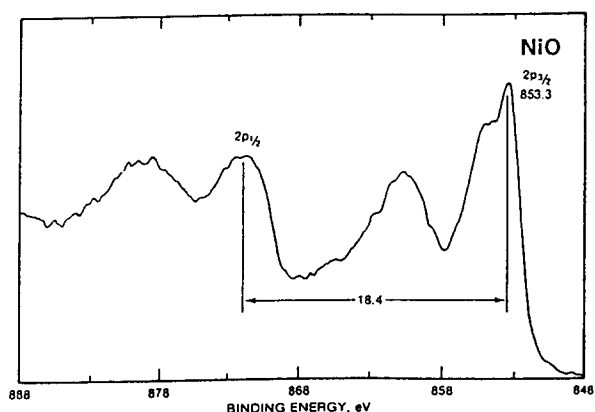

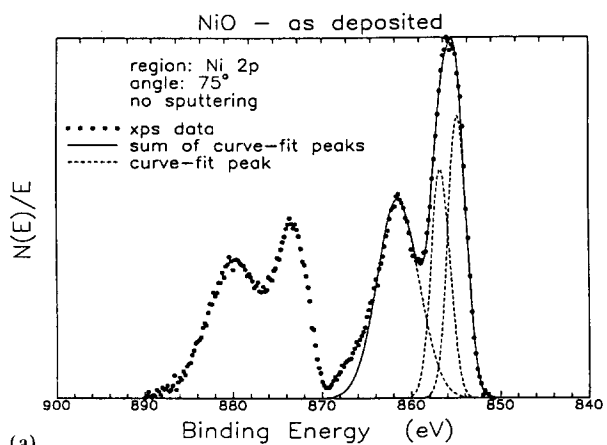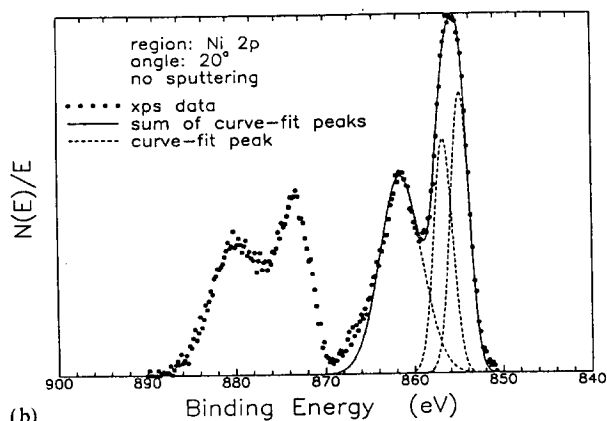Fig. 1. An XPS scan of the surface of sample B.

(a)

(b)

Fig. 2. XPS binding energy of nickel in metallic and oxide form [7].

(a)

(b)

Fig. 3. XPS results of the Ni 2p region for as-deposited samples. The results are shown for 1.31 and 0.35 rad take-off angles. The results from the curve fitting are in Table 3.

of NiO, as shown in Fig. 2(b) [7]. Table 2 shows the binding energy of different oxides and hydroxides of nickel. Nickel hydroxide also shows a single peak (as in nickel metal) at 856 eV [8]. As seen in Fig. 2(b), NiO has a split in its major $2p_{3/2}$ peak.

Figure 3 shows the 2p region for the as-deposited nickel oxide coating (sample B) at two different angles

of observation. Qualitative comparison of the peak position and the shape (formed by the full circles) with that of the NiO peak in Fig. 2(b), shows that the sample mainly consists of nickel oxide. The films were examined at different angles to distinguish between the chemical state of nickel at the surface and slightly deeper into the material. The approximate escape

TABLE 2. X-ray photoelectron spectroscopy binding energies for nickel, NiO, Ni(OH)$_2$ and Ni$_2$O$_3$

Material	Source	XPS binding energy (eV)					
		O 1s	C 1s	Ni $2p_{3/2}$	Satellite	Ni $2p_{1/2}$	Satellite
Ni metal	Powder on tape[a]		285.0	852.7		869.9	
Ni metal	[7]		284.8	852.3		869.7	
Ni(OH)$_2$	Powder on tape[a]	531.2	285.0	856.1			
Ni(OH)$_2$	[8]	531.2	531.2	855.9			
NiO	Powder on tape[a]	529.5	285.0	854.3, 856.2	861.6	872.9	879.8
NiO	[9]	530.0	284.7	854.9, 856.8	862.1		
Ni$_2$O$_3$	[9]	531.8	284.8	857.1	863.0		

[a]The powder samples received from Aldrich Chemical Company were analyzed within a few minutes of opening the containers under ambient conditions.

TABLE 3. Curve fitting results of X-ray photoelectron spectroscopy data (see Figs. 3 and 6), for the Ni $2p_{3/2}$ region of the as-deposited nickel oxide films

Take-off angle (rad)	Band	Binding energy (eV)	FWHM (eV)	Area (counts eV s^{-1})	Ratio of band 1 to band 2
1.31 (no sputtering)	1	854.8	2.5	3.63×10^5	1.23
	2	856.8	2.5	2.95×10^5	
	3	861.6	5.5	5.65×10^5	
0.35 (no sputtering)	1	854.8	2.5	1.97×10^5	1.19
	2	856.8	2.5	1.65×10^5	
	3	861.6	5.5	3.06×10^5	
1.31 (sputtering for 2.5 min)	1	853.4	2.0	7.80×10^5	1.44
	2	855.2	2.5	1.12×10^6	
	3	857.2	3.0	1.07×10^6	
	4	862.0	7.0	2.69×10^6	

length of electrons from nickel for a kinetic energy of 400 eV is 1 nm [10–13].

Qualitatively there do not appear to be any differences in the oxidation state of nickel as a function of depth. To examine this more quantitatively, curve fitting was carried out for the Ni $2p_{3/2}$ peak only. Since there is no unique fit, it was decided to use gaussian peaks with a full width at half-maximum (FWHM) of 2.5 eV. A fit was also carried out for the peak at 862 eV. This is not significant, but the purpose was to subtract its contribution from the Ni $2p_{3/2}$ doublet between 854 and 857 eV (see Table 2). Given these guidelines, we obtained an excellent fit to the data, as seen in Fig. 3 and Table 3. This fit shows no presence of nickel metal in these films. However, the possibility of the presence of Ni(OH)$_2$ at 856 eV still exists. If present, it would be between the two fitted peaks. Moreover, if Ni(OH)$_2$ is indeed present in the films, and it were to change with depth, then the ratio of the two fitted peaks at 854.8 and 856.8 eV would vary. This ratio did not change significantly (Table 3), showing that, if any Ni(OH)$_2$ was present, its contribution remained unchanged with the depth. The absence of Ni(OH)$_2$ could not be confirmed by looking at the O 1s peak, because we had considerable difficulty in separating the oxides of carbon from this peak.

IR spectra on a nickel oxide film and on a nickel hydroxide powder from an earlier publication [14] are shown in Fig. 4. The sharp absorption in Fig. 4(a) at 3640 cm^{-1} is due to nickel hydroxide, and the broad absorption below the peak is probably due to absorbed water. Therefore the broad absorption at around 3500 cm^{-1} in Fig. 4(b) can be assigned to absorbed water or surface hydration and not to a formation of a hydroxide phase. Moreover, since nickel oxide is insoluble in water, it is unlikely that the absorbed water will result in the conversion of nickel oxide to nickel hy-

droxide [15]. An approximate estimate of the concentration of the –OH groups in the nickel oxide films (which results in the absorption between 3500 and 3800 cm^{-1}) can be made. This is done by assuming that the extinction coefficients in the 3500–3800 cm^{-1} region due to –OH groups (because of either hydroxide or hydration from water) and that of Ni–O at 527 cm^{-1} (in hydroxide and oxide) are the same for the samples used in Figs. 4(a) and 4(b). The calculated ratio of –OH peak to Ni–O from these figures in Ni(OH)$_2$ is 1.05, and this ratio for the nickel oxide film is 0.46. Therefore the number of –OH groups in the film is only half that of Ni(OH)$_2$. As argued earlier, the origin of hydroxyl groups in the nickel oxide coating is largely due to absorbed water or surface hydration but is not due to the presence of a bulk hydroxide phase since a sharp absorption at 3640 cm^{-1} is not seen in Fig. 4(b). This calculation shows that in this film the oxygen-to-nickel atomic ratio would be close to 1.5.

X-ray diffraction shows the dominant phase to be polycrystalline nickel oxide (Fig. 5). However, it is difficult to determine whether the crystalline structure is cubic or hexagonal, since the interplanar spacings are almost the same (Table 4) and the peak resolution is poor. The four peaks listed in this table for hexagonal NiO correspond to (101), (212), (110) + (104) and (122) + (110) and for cubic NiO to (111), (200), (220) and (420).

Depth profiling of these layers by sequential sputtering and XPS analysis was not very useful. The curves broadened significantly as seen in Fig. 6 (compare with Fig. 3) and from the results of curve fitting as shown in Table 3. The broadening primarily occurs as a result of the generation of nickel metal (at 862 eV) by sputtering. It has been documented in the literature that, when oxides of heavy metals are sputtered, oxygen is preferentially released. This tendency seems to increase with
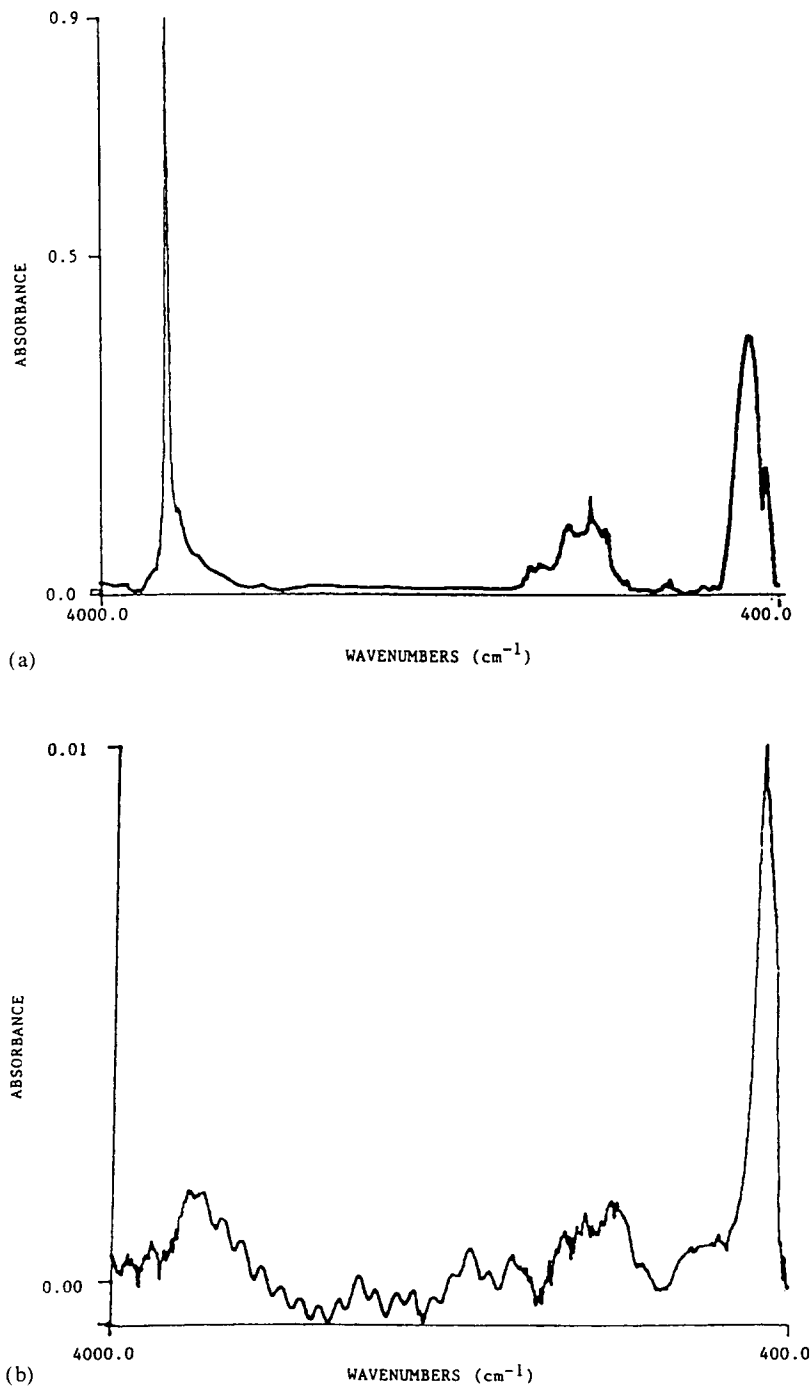
Fig. 4. Fourier transform IR spectrum of (a) powdered nickel hydroxide and (b) as-deposited sample B.

increasing atomic number [24]. When oxides such as Nb_2O_5, Ta_2O_5, TiO_2, HfO_2, ZrO_2 and Al_2O_3 were sputtered with 3 keV Ar^+ ions, all except Al_2O_3 showed a preferential removal of oxygen [25].

The results from RBS on nickel oxide samples are shown in Fig. 7, and the ratio of nickel to oxygen for all samples is shown in Table 5. For all samples, the oxygen-to-nickel atomic ratio was greater than unity,

indicating an oxygen content greater than that expected in stoichiometric NiO. This measured ratio is lower than the ratio of 1.5 obtained by IR and might be explained by water migrating out of the matrix, since RBS experiments were conducted at a pressure of 2.7×10^{-4} Pa. The densities of the films calculated from the RBS results are also shown in this table. The densities have been estimated in two ways: first by
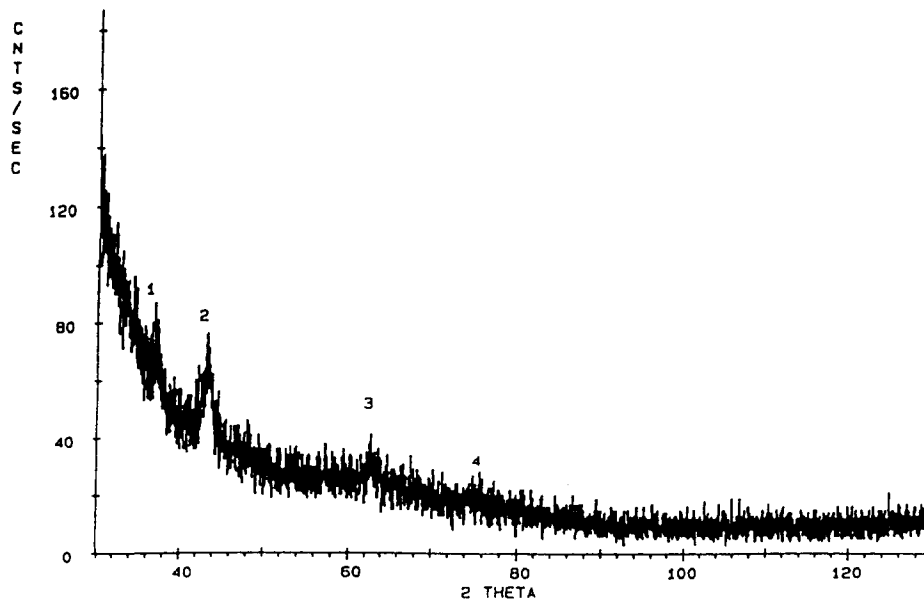
Fig. 5. X-ray diffraction of sample B.

assuming that the number of oxygen atoms is the same as the number of nickel atoms (stoichiometric NiO), and second by accounting for the stoichiometry as determined by RBS.

In summary, the coatings seem to be mainly polycrystalline nickel oxide which have a higher oxygen content than stoichiometric NiO does. The IR results showed that the films contained -OH groups, the source of which could have been water, surface hydration or a non-crystalline hydroxide phase.

3.2. Microstructure

A TEM micrograph of sample A (all samples were deposited on carbon-coated copper grids unless mentioned otherwise) is shown in Fig. 8. The average grain size is 4 nm. To confirm that the features do not change with the contrast transfer function of the microscope, micrographs were taken at two objective apertures of

120 and 60 μm, and a through-focus series was also done, as shown in Fig. 9. Since in all these micrographs the features do not change and their sizes are similar, one can conclude that they represent the sample morphology. The different shades of grey are due to the difference in the orientation of the crystals. One can see boundary lines between each of the grains and also a much wider boundary around clusters of crystals 60–100 nm in size; the boundary could be as wide as 10 nm. This figure shows that these samples could have large surface areas and the spaces between the crystallites are large enough for ionic diffusion of OH^- ions since their size is only 0.14 nm [26].

Electron diffraction patterns from sample A are shown in Fig. 10. These two patterns are from the same area of the sample but have been exposed for different times to yield better resolution and more lines. These lines can be indexed to a cubic NiO phase. This has also

TABLE 4. d spacings of the most intense peaks of nickel oxide and hydroxide compared with the data for the as-deposited nickel oxide coatings

d spacing (nm)

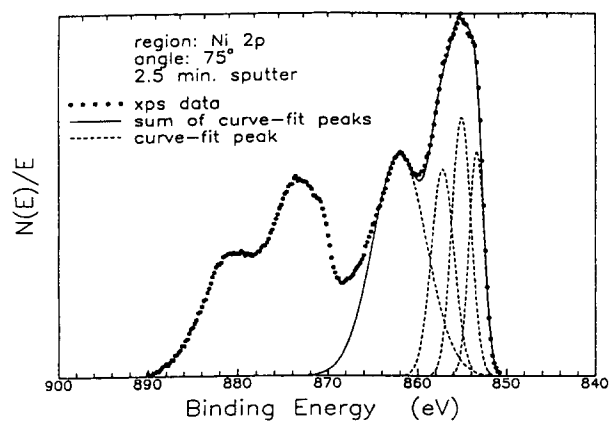| As-deposited film	NiO, hexagonal [16]	NiO, cubic [17]	Nickel hydroxide hydrate, hexagonal [18]	β-Ni(OH)₂, hexagonal [19]	Ni₂O₃, hexagonal [20]	NiOOH, orthorhombic [21]	β-NiOOH hexagonal [22]	γ-NiOOH hexagonal [23]
0.243	0.241	0.240	0.760	0.461	0.280	0.317	0.483	0.690
0.209	0.209	0.209	0.374	0.271	0.230	0.248	0.241	0.343
0.148	0.148	0.148	0.266	0.233	0.202	0.239	0.140	0.237
	0.126	0.126	0.255	0.175	0.177	0.169		0.209
	0.093	0.093	0.231	0.156	0.162	0.161		0.177
			0.219			0.140		0.141
			0.155					0.137

Fig. 6. XPS spectrum of Ni 2p region for sample B that has been sputtered for depth profiling.

Fig. 7. RBS analysis of sample B.

(a)

(b)

Fig. 8. TEM micrographs of sample A. The objective aperture for (a) was 120 μm and for (b) 60 μm.
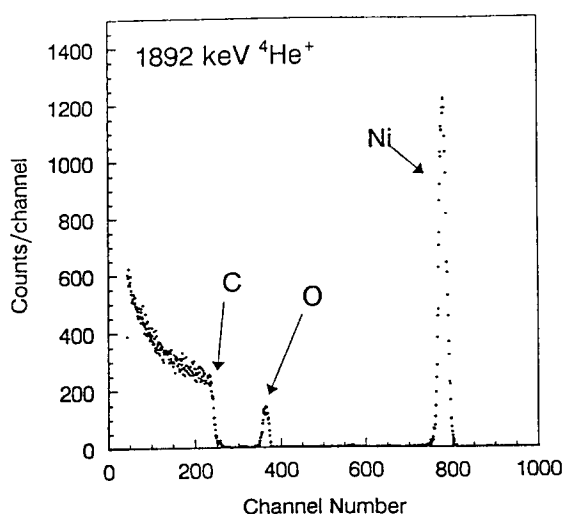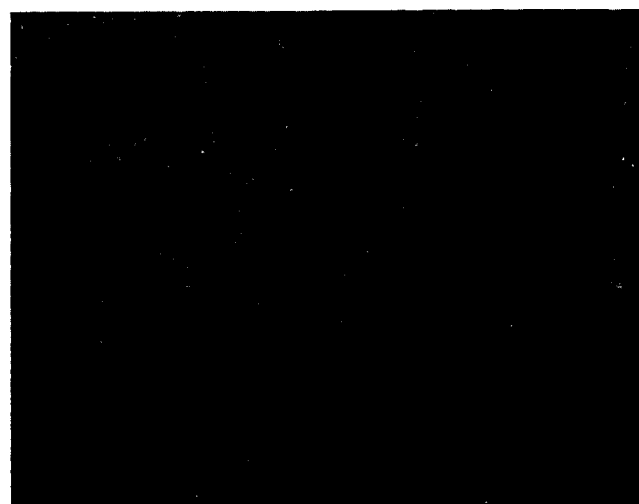
been confirmed in an earlier study on evaporated nickel oxide films [27]. A dark field micrograph obtained by blocking the transmitted light is seen in Fig. 11. When this sample is tilted by 0.52 rad, the bright field image becomes a little fuzzy but still has all the same characteristics (Fig. 12), and the diffraction pattern does not show any differences from Fig. 10. This shows that the

orientation of the crystallites is random in the plane of the film and through the thickness.

For sample B, Fig. 13 shows two bright field micrographs taken at different magnifications and an electron diffraction pattern. The crystallite size is larger with an average size of 5.4 nm, and no wide boundaries or large

TABLE 5. Rutherford backscattering spectroscopy results on nickel oxide films deposited on carbon substrates

Sample	Number of Ni atoms per area ($\times 10^{-15}$ atoms cm^{-2})	O-to-Ni ratio	Calculated density of the films[a] (kg m^{-3})	
			NiO	NiO$_{1+x}$
A	108 ± 3	1.34 ± 0.009	2700	2900
B	161 ± 5	1.22 ± 0.006	4100	4300
C	171 ± 5	1.26 ± 0.004	5000	5300

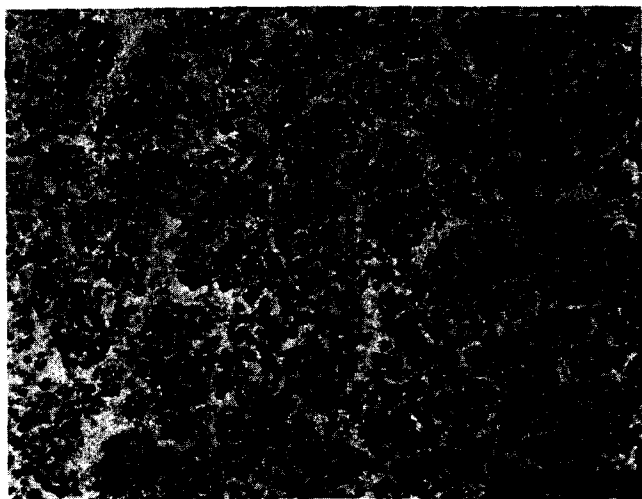[a]The bulk density of crystalline NiO is 6670 kg m^{-3}.
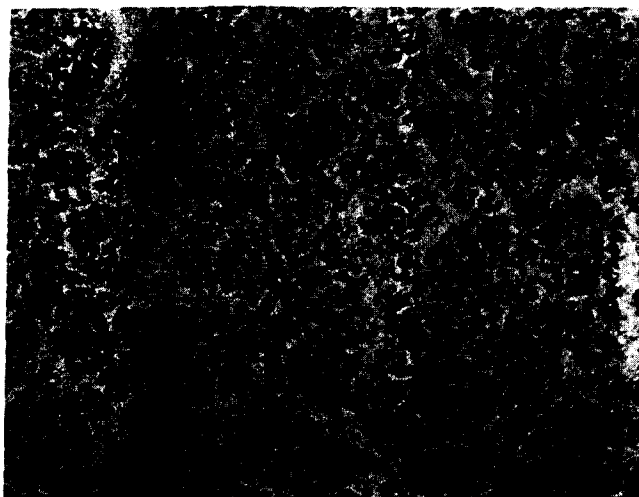
(a)

(b)

(c)

Fig. 9. Through-focus series of TEM micrographs of sample A: (a) underfocus; (b) focus; (c) overfocus. The objective aperture size was 120 μm.
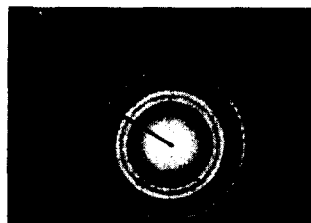
Fig. 10. Electron diffraction patterns from sample A. Both are from the same sample but taken at different exposures to show the details in the pattern.
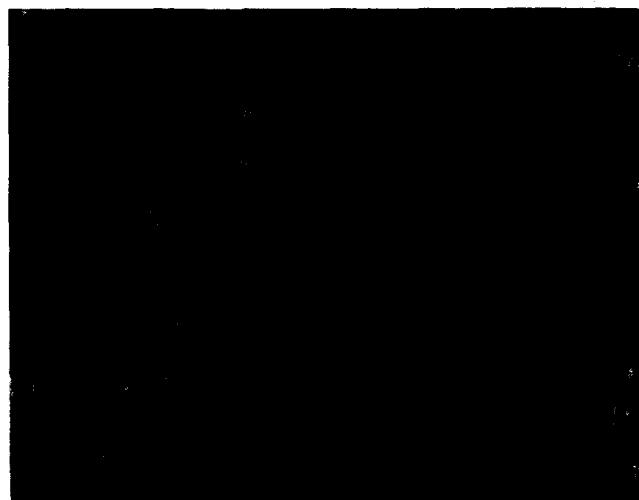
Fig. 11. A dark field image of sample A. This was made by blocking the transmitted beam.

clusters are visible. The narrow boundaries indicate that the space between the crystallites is smaller. Since there is no change in the electron diffraction pattern, one concludes that both sample A and sample B are primarily crystals of cubic NiO. To determine whether the structures on carbon-coated grids truly represent the structure of nickel oxide deposited on ITO-coated glass, a TEM micrograph of the nickel oxide coating scraped from an ITO surface was taken. This is shown in Fig. 14, which was determined to be qualitatively similar to the other micrographs. A cross-section of nickel oxide deposited on ITO-coated glass in bright field and dark field is shown in Fig. 15. One can see channels (or a fibrillar morphology) between columns of crystallites. Also, each fibril or column is not a single crystallite but
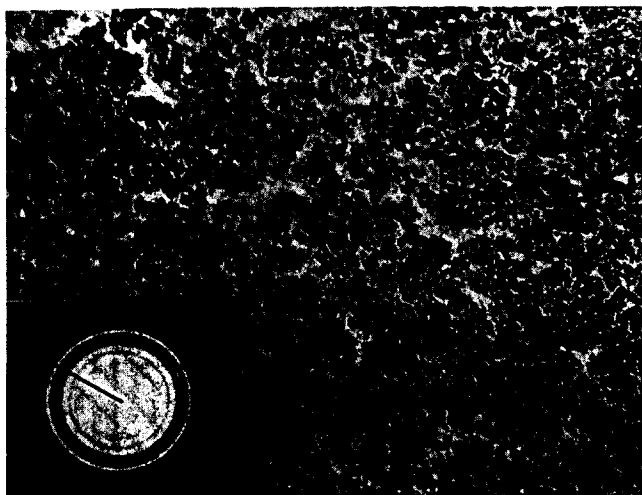
Fig. 12. TEM micrograph and an electron diffraction pattern of sample A. The sample was tilted by 0.52 rad along the horizontal axis, passing through the plane of the film.
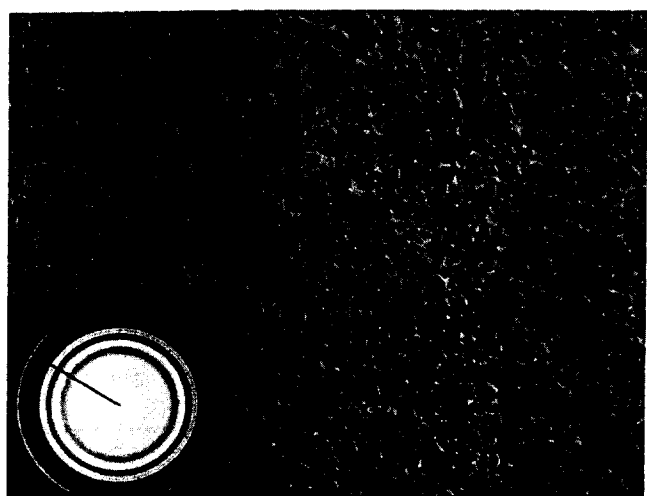

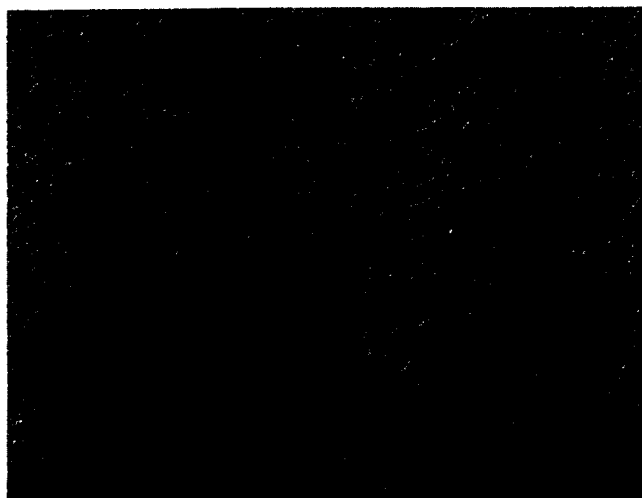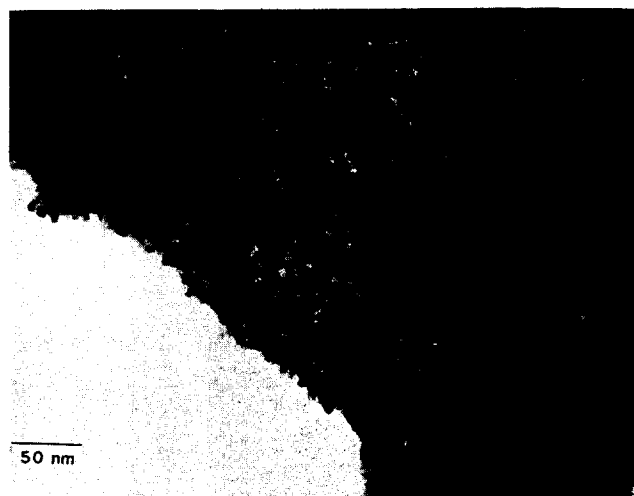Fig. 14. TEM micrograph of sample B removed mechanically from an ITO-coated glass substrate.

(a)

Fig. 13. TEM micrographs at different magnifications and an electron diffraction pattern for sample B.
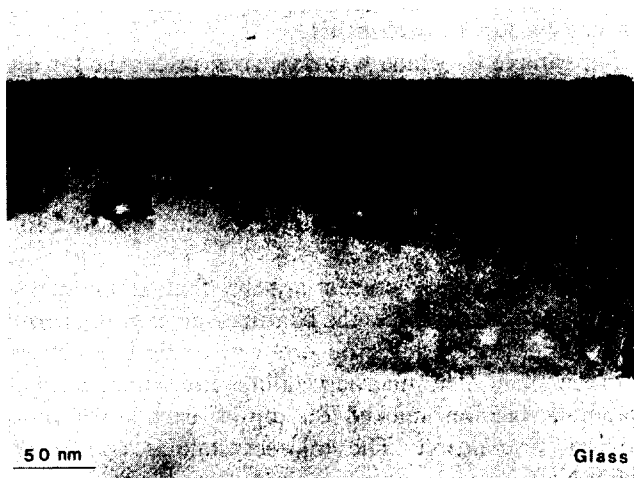

(b)

Fig. 15. TEM cross-sectional view of sample B on an ITO-coated glass substrate in (a) bright field and (b) in dark field.

Fig. 16. TEM micrograph and an electron diffraction pattern from sample C.

consists of a number of randomly oriented crystallites stacked on top of each other.

For sample C, which was deposited under the lowest pressure conditions, one finds that not only has the crystal size become larger (about 6.5 nm) but also the boundaries between them are much sharper and narrower (Fig. 16). The electron diffraction pattern reveals that the crystal structure is similar to that observed for the other samples.

From the microstructure it appears that, as the deposition pressure increases, the coatings increase in porosity owing to decreasing grain size with wider boundaries between them. The microcrystallites are arranged in a columnar fashion stacked on top of each other in a random orientation. The microcrystallites consist of cubic NiO.

3.3. Model

To understand the oxygen-rich stoichiometry and the influence of microcrystallites on the electrochromic behavior of these films, the following is proposed. It is assumed that the columns seen in the microstructure of sample A (Fig. 15) consist of 4 nm cubes stacked on one another. Figure 17(a) shows a unit cell of close-packed (f.c.c.) crystalline NiO with a lattice constant of 0.418 nm
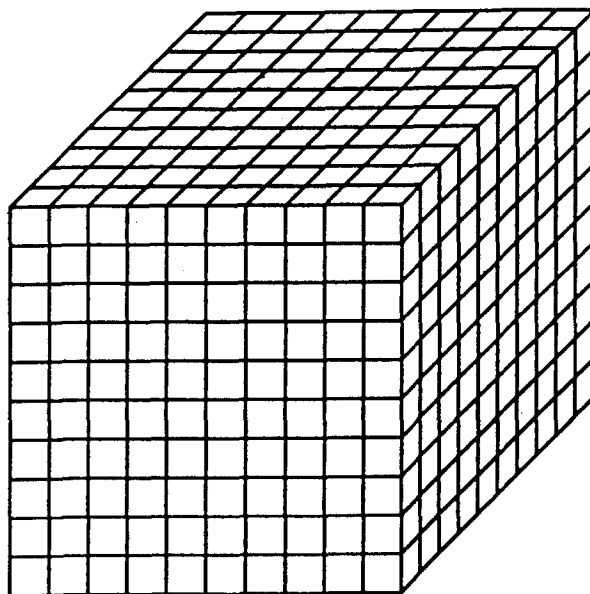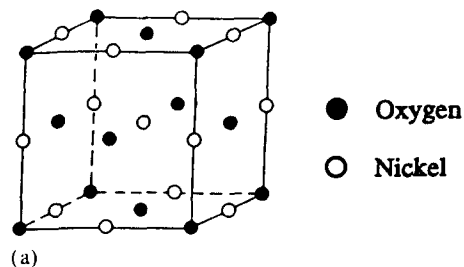

Fig. 17. (a) A unit cell of nickel oxide; (b) a microcrystallite consisting of 1000 unit cells.

[17]. As seen in this figure, nickel atoms inside the crystal would be in the center of an octahedron formed by its near-neighbor oxygen atoms. Figure 17(b) shows a crystallite with a dimension of 4.18 nm, i.e. ten unit cells on each side. This crystallite is of approximately the same size as observed in the TEM micrograph of sample A. A quick calculation shows that the total nickel atoms in this cube is 4000, of which 926 are surface atoms and 3024 are bulk atoms. Therefore the ratio of bulk to surface atoms in this sample is 3.1. The results of similar calculations on samples A and B respectively for crystallite sizes of 5.4 nm and 6.7 nm are in Table 6. One could

TABLE 6. Calculated values of the number of surface nickel oxide molecules to the bulk molecules

Sample	Deposition pressure of the films (Pa)	Average grain size (nm)	Ratio of bulk to surface molecules	Calculated O-to-Ni ratio
A	0.067	4.0	3.1	1.25
B	0.013	5.4	4.1	1.20
C	2.7×10^{-4}	6.7	5.1	1.17

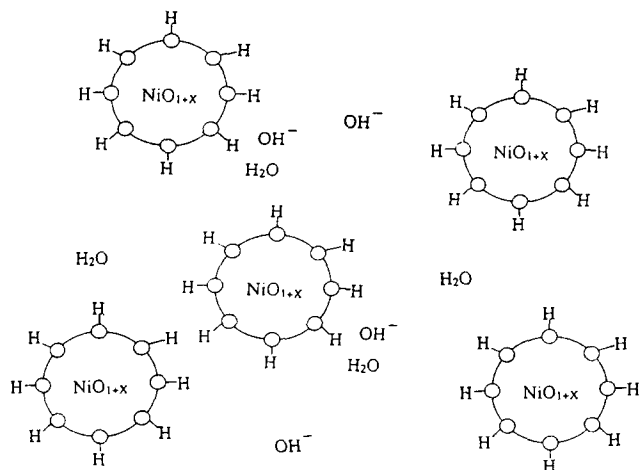A nominal film thickness of 45 nm has been assumed.

Fig. 18. Proposed structure of nickel oxide films, showing that the surface of the microcrystallites is hydrated and the interparticle space contains water and hydroxyl ions.

further extrapolate these results to calculate the stoichiometry of the films, by assuming that the coordination number of nickel atoms on the surface is the same as in the bulk, and that the coordination of nickel on the surface is completed by bonding to an –OH group. This is not a hypothetical assumption because, as shown by IR analysis (Fig. 4(b)), these coatings appear to be hydrated. The excess charge on the surface of these particles imposed by a fixed coordination number is balanced by hydrating the surface. The pH at which the particle is neutrally charged is called the point of zero charge (PZC). Since the PZC for nickel oxide is 10.3 [28], one could expect (as shown in Fig. 18) the surface of a nickel oxide to be mainly covered with hydroxyl groups compensated by OH^- groups and water in the interparticle space [29]. However, the presence of hydroxyl groups on the surface does not imply the presence of nickel hydroxide, since no nickel atom is completely coordinated with only hydroxyl groups. Also the IR spectra of the nickel oxide film does not show the sharp peak present in nickel hydroxide at 3640 cm^{-1}. The stoichiometry of each crystallite and hence the films is then calculated by allowing for the excess oxygen (i.e. from the hydroxyl groups) which is needed to hydrate the surface of a nickel oxide crystallite. The results of this calculation for all the samples are shown in Table 6. The numbers in this table compare quite favorably with the experimentally determined stoichiometry by RBS in Table 5.

Therefore it is proposed that these films are composed of crystalline nickel oxide columns which extend through the thickness of the film. Each of these columns is composed of microcrystals stacked on each other in a random orientation. Further, owing to a large surface area and a high PZC of these oxides, the surface is hydrated, which results in their oxygen-rich

stoichiometry. The surface hydration and high PZC lead to hydroxyl ions dispersed in the water in the interparticle space.

3.4. Electrochemical measurements

Figure 19 shows the results of cyclic voltammetry on the three samples. These experiments were carried out in 1 N KOH at a sweep rate of 50 mV s^{-1}. In each of the samples, the voltammogram changes with the number of cycles. An increase in anodic and cathodic current is seen, showing that the number of species that are being reduced or oxidized increases with time. This can happen if the surface area of the electrode increases
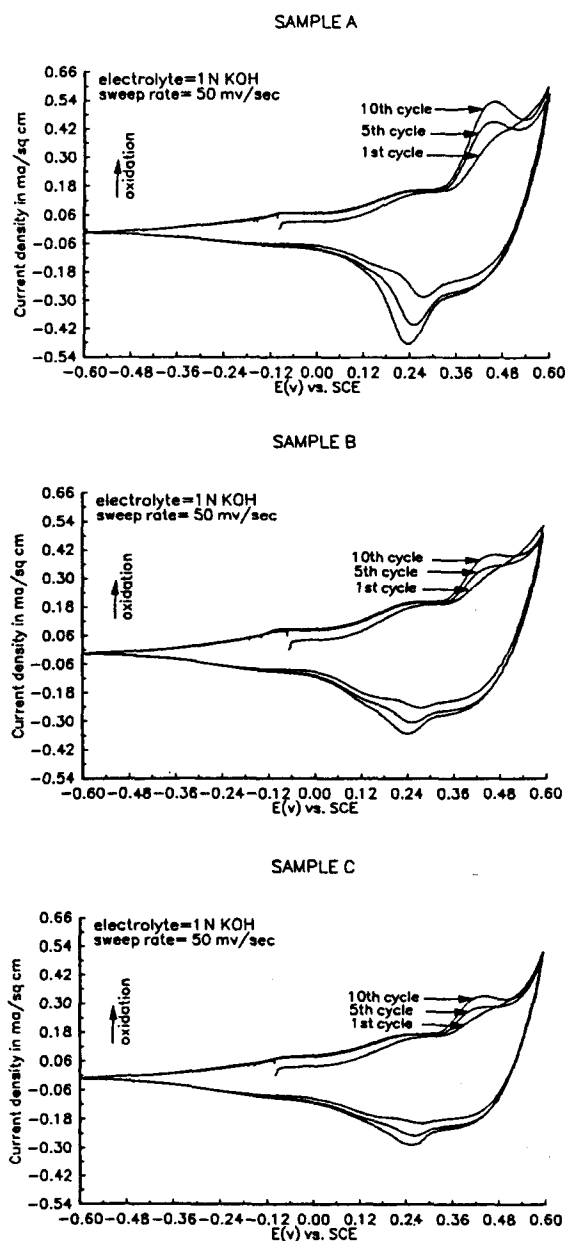

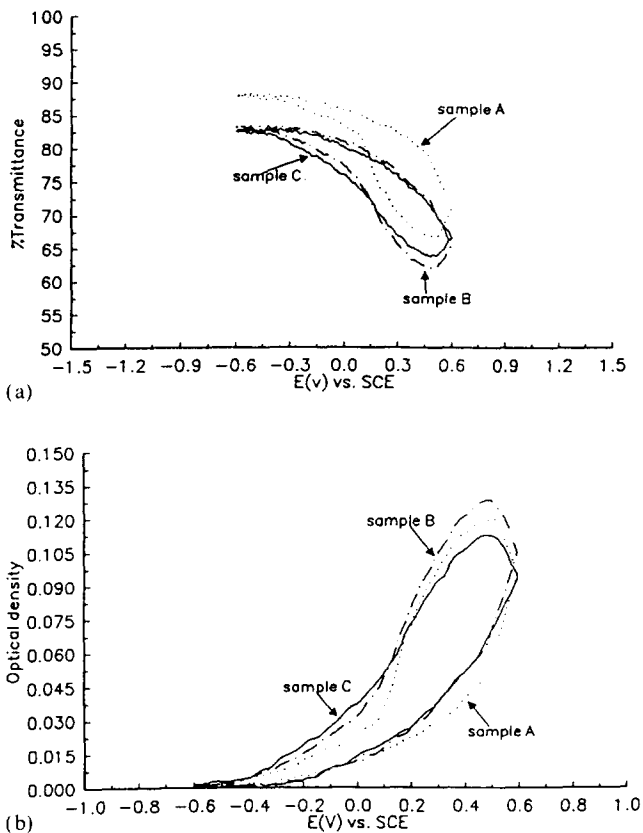Fig. 19. Cyclic voltammograms $(C-V)$ on the nickel oxide films.

(a)

(b)

Fig. 20. Change in the optical properties at 550 nm during the tenth $C-V$ cycle (see Fig. 19) of the films.

Fig. 21. Potential (with respect to a SCE) time profile used to color the films in 1 M KOH with platinum mesh as the counterelectrode.

owing to the corrosion caused by the cycling in the electrolyte. The change in the redox currents is largest for sample A, followed by sample B and then by sample C, which may be a result of the surface area, which is highest for sample A, and in sample C it is lowest. The corresponding change in the optical transmission of the sample at the tenth cycle at 550 nm is shown in Fig. 20(a). Sample A shows a response that is shifted on the y axis with respect to samples B and C. The data can also be normalized to the most transmitting state and reported as optical density as shown in Fig. 20(b). The observed shift is due to the substantially lower density of sample A (see Table 5), which results in a lower refractive index. The electrochromic properties of the films colored by a step potential were measured after the sample had been subjected to 10 cycles in KOH (Fig. 19). The samples were colored by applying step voltages of 0.46 V(SCE) for coloration and −0.44 V(SCE) for bleach, as shown in Fig. 21. The results of the kinetics of color change at 550 nm and charge consumed are shown in Fig. 22. The data were taken after zeroing the optical contribution from the cuvette, electrolyte and platinum mesh. The spectral characteristics of these films as shown in Fig. 23 were measured after coloring or bleaching the samples in the
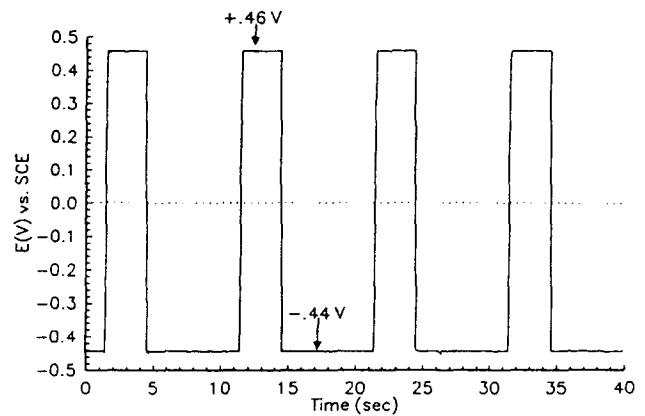
liquid electrolyte, followed by washing, drying and inserting only the samples in the spectrometer. The kinetics data for coloration in Fig. 22 are comparable for all the three samples, but the charge consumed is highest for sample A and decreases for sample B and then further decreases for sample C. The optical efficiency at 550 nm is the slope of the curve obtained by plotting optical density vs. charge consumed. The results are shown in Table 7.

Films deposited at the highest pressure have the lowest coloring efficiency. Since we know the number of nickel atoms per square centimeter in these films from the RBS experiments and the charge consumed from Fig. 22, we can also calculate the average number of hydroxyl ions consumed (or electrons ejected) to oxidize each molecule of the oxide in the film. The optical density in the colored state in Fig. 22 at 550 nm is approximately 0.10. The average number of electrons needed to bring 100 oxide molecules to a coloration level corresponding to an optical density of 0.10 is given in Table 7. This shows that the coloring efficiency for the film deposited in a high vacuum (sample C) is about twice that for sample A, which is deposited under higher pressure conditions.

Although the electrochromic properties of these films are measured in 1 N KOH solution, KOH is rarely used as the electrolyte in an electrochromic device because of the poor chemical stability of nickel oxide films needed for extensive cycling. The cyclic voltammograms showed that considerable changes were taking place in the films at least up to 10 cycles, and these changes continue until there is no electrochemical activity. Since the electrochromic properties were measured after 10 $C-V$ cycles, the film morphology and chemistry are probably quite different from those in the as-deposited state. The results reflect modifications caused by the corrosive nature of the KOH. One would expect to see
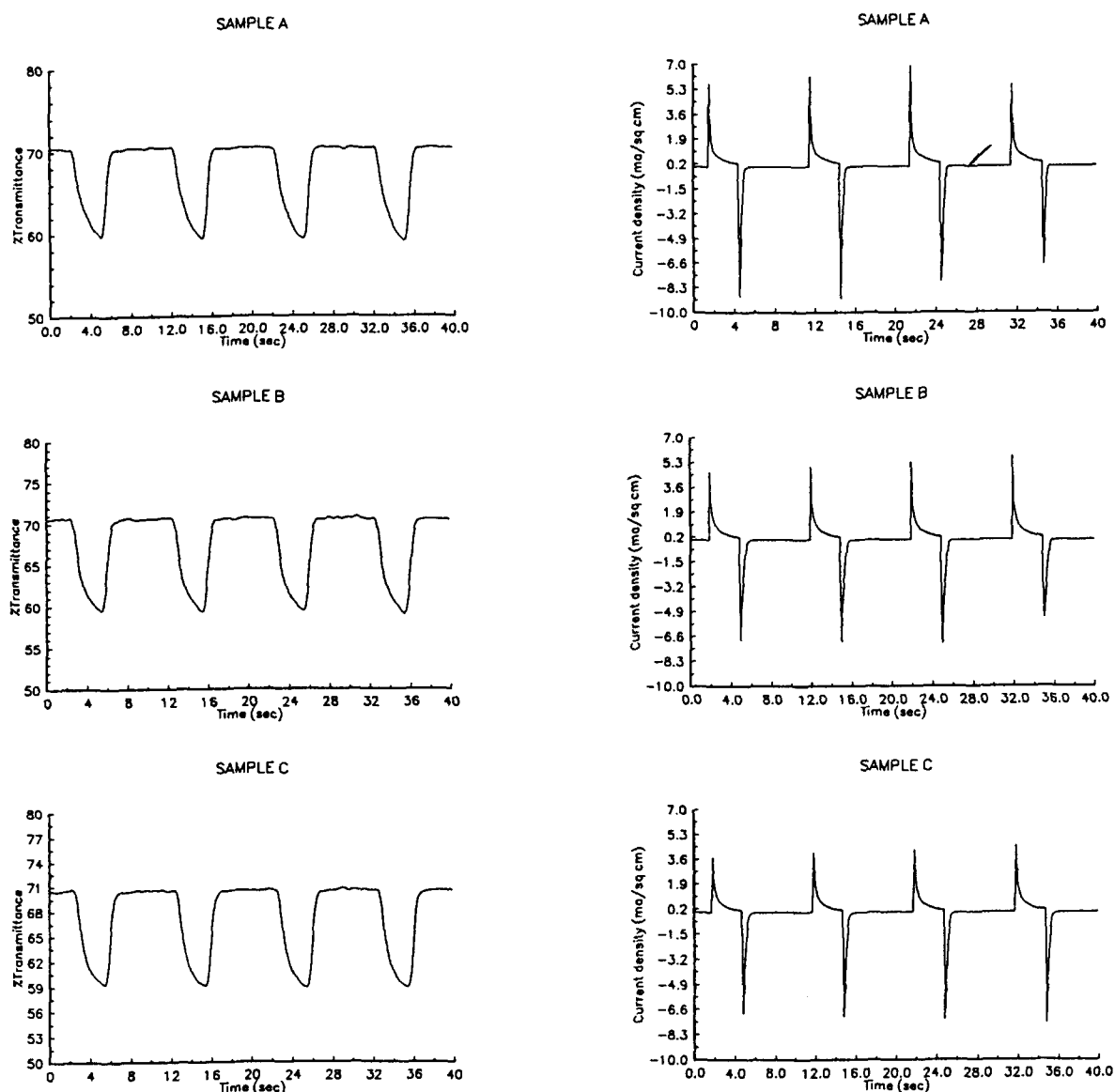
Fig. 22. Percentage transmittance at 550 nm and the charge consumed when these films are cycled under conditions shown in Fig. 20.

a large difference in the performance of the electrochromic devices if these films had been incorporated into thin film solid state or laminate devices.

We can now draw some conclusions about the coloration reactions that occur (see eqns. (1)–(3)). Our results indicate that $Ni(OH)_2$ is not present at detectable levels in as-deposited films, but the films may be hydrated and the microcrystallites may be covered with –Ni–OH bonds on the surface. This is not the same as $Ni(OH)_2$ since we believe that nickel atoms are not present in eightfold coordinations with –OH as required by the hydroxide, but it is possible that some hydroxide may have been generated because of the C-V cycling. OH^- ions initially present between the microcrystallites may be injected into the matrix to

form colored species and, since the PZC for nickel hydroxide is quite basic (about 11.1 [28]), compensating hydroxyl ions from the electrolyte will maintain the charge neutrality of the oxide layer. If we want to associate the electrochromic phenomena with the surface of the microcrystallites, then at least the number of surface atoms to the number of NiO molecules participating in the reaction should be compared. Since there are up to 20% surface nickel atoms (Table 6), and Table 7 shows that only 6–12% of the total nickel atoms participate in the electrochromic reaction, the numbers indicate that the surface molecules may be able to provide for all the active sites; however, sample A, which has the maximum surface, needs twice the number of the oxidizing species that sample C does.
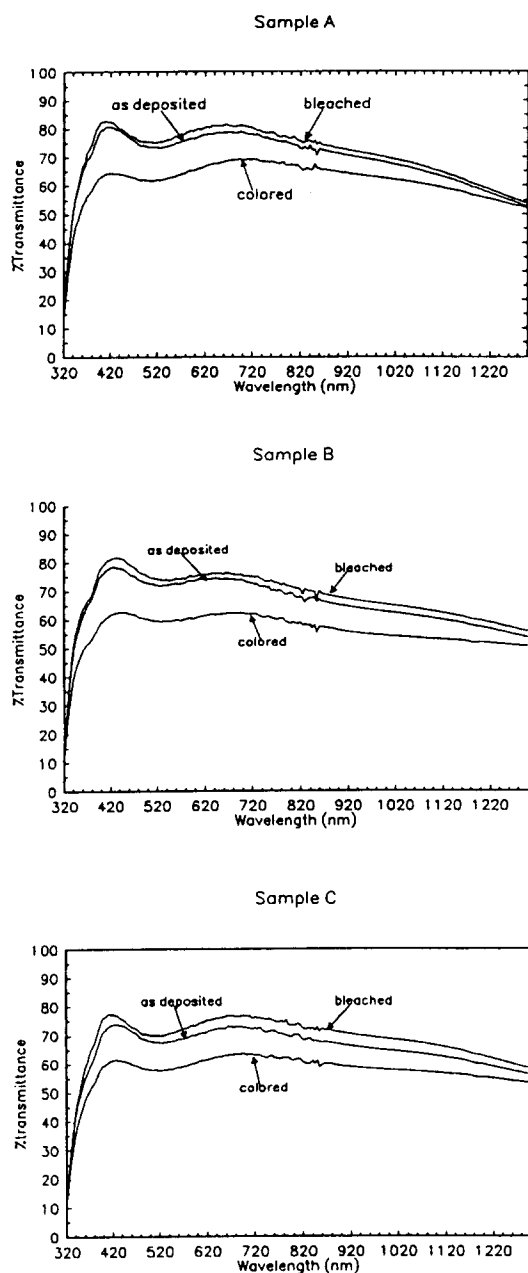
Sample A

Sample B

Sample C

Fig. 23. Spectral response to the films in the colored and the bleached states.

Therefore the presence of a large surface results in poorer efficiency, with no appreciable difference in the depth of coloration (Fig. 22). This indicates that the active sites are not likely at the surface. The bulk, as seen by X-ray diffraction, consists largely of nickel oxide phase. Therefore we conclude that the active sites are in bulk nickel oxide and eqn. (1) is the likely electrochromic reaction taking place in these films. For nickel oxide coatings to be electrochromic, we may need the surface hydration and the intercrystalline OH⁻ for a high ionic (hydroxyl ion) conductivity.

TABLE 7. Optical efficiency

Sample	Coloring efficiency $(cm^2\,C^{-1})$ at 550 nm	Electrons per 100 Ni atoms to obtain an optical density of 0.10 at 550 nm
A	32.5	17.8
B	36	10.9
C	40	9.1

4. Conclusions

The electron-beam-evaporated nickel oxide coatings were found to consist of polycrystalline nickel oxide. The packing and the size of the crystallites in the film were dependent on the pressure in the chamber during their evaporation. The crystallites (4–6.7 nm in size) were packed on top of each other, resulting in columns extending through the thickness of the coating. The orientation of the crystals in any given column was uncorrelated. The as-deposited films did not seem to contain nickel hydroxide, but the surfaces of the microcrystallites were hydrated, which resulted in greater oxygen content than that expected in stoichiometric NiO. The intercrystalline region consists of water and hydroxyl ions. The electrochromic properties of the films in KOH solution are influenced by the film microstructure, but we expect that variations in the nickel oxide microstructures would show larger differences in device performance. The most likely coloration mechanism in these films is by the oxidation of nickel oxide to nickel oxyhydroxide.

Acknowledgment

References

1 S. E. Selkowitz and C. M. Lampert, *Large-Area Chromogenics: Materials and Devices for Transmittance Control*, Society of Photo-optical Instrumentation Engineers, Bellingham, WA, 1990, p. 22.
2 N. Lynam and A. Agrawal, *Large-Area Chromogenics: Materials and Devices for Transmittance Control*, Society of Photo-optical Instrumentation Engineers, Bellingham, WA, 1990, p. 46.
3 P. Delichere, S. Joiret and A. Hugot-Le Goff, *J. Electrochem. Soc., 135* (1986) 1856.
4 S. I. Cordoba-Torressi, A. Hugot-Le Goff and S. Joiret, *J. Electrochem Soc., 138* (1991) 1554.
5 C. M. Lampert, T. R. Omstead and P. C. Yu, *Proc. Soc. Photoopt. Instrum. Eng., 562* (1986) 16.
6 M. K. Carpenter, R. S. Conell and D. A. Corrigan, *Sol. Energy Mater., 16* (1987) 333.

7 C. D. Wagner, W. M. Riggs, L. E. Davis and J. F. Moulder, *Handbook of X-ray Photoelectron Spectroscopy*, PHI, Eden Prairie, MN, 1979.

8 N. S. McIntyre, T. E. Rummery, M. G. Cook and D. Owen, *J. Electrochem. Soc.*, *123* (1976) 1164.

9 K. T. Ng and D. M. Hercules, *J. Phys. Chem.*, *80* (1976) 2094.

10 C. J. Powell, *Surf. Sci.*, *44* (1974) 29.

11 M. P. Seah, *Surf. Sci.*, *32* (1972) 703.

12 I. Lidau and W. E. Spicer, *J. Electron Spectrosc.*, *3* (1974) 409.

13 C. R. Brundle, *J. Vac. Sci. Technol.*, *11* (1974) 212.

14 N. R. Lynam and H. R. Habibi, *Proc. Soc. Photo-opt. Instrum. Eng.*, *1016* (1988) 63.

15 Joint Committee on Powder Diffraction Standards, *Powder Diffraction File*, International Center for Diffraction Data, Swarthmore, PA, 1972, Card 22-1189.

16 R. I. Razouk and R. S. Mikhail, *J. Phys. Chem.*, *62* (1958) 920.

17 Joint Committee on Powder Diffraction Standards, *Powder Diffraction File*, International Center for Diffraction Data, Swarthmore, PA, 1954, Card 4-0835.

18 V. H. Bode, K. Dehmelt and J. Witte, *Z. Anorg. Allg. Chem.*, *366* (1969) 1.

19 Joint Committee on Powder Diffraction Standards, *Powder Diffraction File*, International Center for Diffraction Data, Swarthmore, PA, 1964, Card 14-117.

20 P. S. Agrawal and A. Goswami, *J. Phys. Chem.*, *65* (1961) 2105.

21 S. Chenavas, J. C. Joubert and J. J. Capponi, *J. Solid State Chem.*, *6* (1973) 1.

22 V. O. Glemser and J. Einerhand, *Z. Anorg. Allg. Chem.*, *261* (1950) 47.

23 V. O. Glemser and J. Einerhand, *Z. Anorg. Allg. Chem.*, *261* (1950) 43.

24 D. Briggs, in C. R. Brundle and A. D. Baker (eds.), *Electron Spectroscopy, Theory and Applications*, Academic Press, New York, 1979, p. 305.

25 S. Hoffman and J. M. Sanz, *J. Trace Microprobe Techn.*, *1* (1982–1983) 213.

26 A. R. West, *Basic Solid State Chemistry*, Wiley, New York, 1988, p. 80.

27 C. M. Lampert and R. S. Caron-Popowich, *Proc. Soc. Photo-opt. Instrum. Eng.*, *1149* (1989) 56.

28 G. A. Parks, *Chem. Rev.*, *65* (1965) 177.

29 A. Clearfield, *Solid State Ion.*, *46* (1991) 35.